PAPER

A gyrokinetic perspective on the JET-ILW pedestal

View the article online for updates and enhancements.

A gyrokinetic perspective on the JET-ILW pedestal

D.R. Hatch, M. Kotschenreuther, S. Mahajan, P. Valanju and X. Liu

Institute for Fusion Studies, University of Texas at Austin, Austin, TX 78712, USA

E-mail: drhatch@austin.utexas.edu

CrossMark

Abstract

JET has been unable to recover historical confinement levels when operating with an ITER-like wall (ILW) due largely to the inaccessibility of high pedestal temperatures. Finding a path to overcome this challenge is of utmost importance for both a prospective JET DT campaign and for future ITER operation. Gyrokinetic simulations (using the GENE code) quantitatively capture experimental transport levels for a representative experimental discharge and qualitatively recover the major experimental trends. Microtearing turbulence is a major transport mechanisms for the low-temperature pedestals characteristic of unseeded JET-ILW discharges. At higher temperatures and/or lower ρ_*, we identify electrostatic ITG transport of a type that is strongly shear-suppressed on smaller machines. Consistent with observations, this transport mechanism is strongly reduced by the presence of a low-Z impurity (e.g. carbon or nitrogen at the level of $Z_{\text{eff}} \sim 2$), recovering the accessibility of high pedestal temperatures. Notably, simulations based on dimensionless ρ_* scans recover historical scaling behavior except in the unique JET-ILW parameter regime where ITG turbulence becomes important. Our simulations also elucidate the observed degradation of confinement caused by gas puffing, emphasizing the important role of the density pedestal structure. This study maps out important regions of parameter space, providing insights that may point to optimal physical regimes that can enable the recovery of high pedestal temperatures on JET.

Keywords: pedestal, H-mode, transport, shear suppression, JET, gyrokinetics, turbulence

(Some figures may appear in colour only in the online journal)

1. Introduction

The H-mode pedestal—the steep gradient region of the edge transport barrier—is central to both confinement and material considerations in tokamaks. Since the installation of an ITER-like wall (ILW) [1, 2] on JET, high pedestal temperatures have become inaccessible resulting in a significant loss of confinement [3–8]. Good confinement must be recovered in order to achieve substantial fusion power in a prospective renewal of DT operation. Moreover, successful operation with ITER materials must be demonstrated on present-day experiments in order to transition with confidence to ITER. In this paper we describe simulations using the GENE [9, 10] code that reproduce the major trends observed in JET-ILW discharges, thereby constructing a conceptual framework for the transport dynamics that may underly the puzzling changes in pedestal properties. Building such a framework has another equally important objective—to discover regimes that may restore or even improve on historically accessible pedestal temperatures and confinement.

To date, pedestal structure has been interpreted almost solely through the lens of MHD stability. Such a paradigm has proven valuable in explaining aspects of pedestal behavior throughout a wide range of devices [11–14]. The pre-ELM plasma is typically found near a peeling-ballooning (ideal MHD) stability limit. The nature of the pedestal transport provides a constraint on pedestal evolution that ultimately determines the operating point at which the plasma becomes unstable to peeling-ballooning modes and an ELM is triggered. The EPED model [13, 14], for example, appeals to kinetic ballooning modes (KBM) as the constraining transport mechanism and the KBM stability limit (essentially a second

MHD limit) is used in conjunction with the peeling ballooning limit to predict pedestal properties.

In this work, we highlight the role of non-MHD (i.e. not KBM) transport mechanisms—which we will call drift-type—in determining pedestal properties. Drift-type transport mechanisms are described best by gyrokinetic models. Several fundamental as well as practical considerations compel an examination of pedestal dynamics that goes beyond MHD:

(1) A purely MHD analysis of the pedestal assumes that the drift-type turbulent transport is a minor player in determining pedestal properties—an assumption that appears to be incomplete in a substantial class of present-day parameter regimes, and is certainly not assured as we progress towards larger machines with more challenging performance goals. The addition of drift-type transport to the investigative repertoire (in order to develop a more complete picture of pedestal dynamics) would seem like a theoretical necessity.

(2) A distinguishing property of JET-ILW pedestals—an apparently unavoidable and largely unexplained constraint on pedestal temperature as opposed to pressure—is an excellent illustrative example. Within the MHD paradigm, the pedestal stability is determined mostly by the pressure profile; distinctions between density and temperature (through, for example, collisionality effects as manifest in the bootstrap current) play a rather subsidiary role. Thus the clamping down of the temperature profile in particular is likely to require an extra-MHD explanation.

(3) An MHD model, though quite adequate for assessing the stability of a pedestal, can tell us little about the heating power required to achieve it. Once the L-H threshold power is exceeded, the pre-ELM plasma pressure (or β) varies substantially with heating power. MHD can say little about what value of β can be achieved with a given heating power. As a simple illustration [15], describes two JET-ILW discharges whose MHD stability properties accommodate the same pedestal-top pressure (i.e. stored energy) but require widely differing heating power (resulting in different confinement times) due to a shift in the relative density and temperature profiles. In other words, different MHD stability limits are reached depending on the applied heating power—a distinction that cannot be addressed by MHD stability considerations.

When a gyrokinetic transport theory is added to MHD, the composite perspective will rectify several shortcomings of the prevailing paradigms: (1) the properties of gyrokinetic drift-type turbulence depend intrinsically and sensitively on distinctions between temperature and density profiles, and (2) gyrokinetics explicitly models transport and thus speaks directly to confinement. In light of these observations, we stress that gyrokinetics will be an indispensable complement to the MHD stability paradigm in understanding pedestal dynamics (see section 3 for more discussion of the interplay between drift-type transport and MHD stability). Indeed, as is shown in this paper, the picture revealed in our gyrokinetic simulations offers potential explanations for the major unexplained trends observed on JET-ILW.

The preliminary results described in this paper are consistent with the following important JET-ILW observations: (1) the inaccessibility of high pedestal temperatures, (2) the degradation of confinement with gas puffing, (3) the partial recovery of confinement with impurity seeding, and (4) the stronger propensity for metal-wall confinement issues on JET in comparison with ASDEX Upgrade (AUG) [16] (JET accessing lower values of ρ_* than AUG). The concepts invoked in this paper are by no means exhaustive (detailed MHD stability considerations, aspects of divertor operation, details of impurity ionization and radiation, etc are not included), but they do add a new perspective on the mechanisms that impact pedestal properties; this framework should not only enable a better interpretation of JET-ILW pedestal dynamics but may also aid in guiding solutions for JET-ILW and future devices.

The transport mechanisms identified in this study can be broadly classified in two categories: those that deviate only weakly from gyroBohm scaling and those that deviate strongly from gyroBohm. This paper outlines the ways in which both classes of transport affect metal-wall confinement. Microtearing modes (MTM) and electron temperature gradient (ETG) turbulence fall in the former category. MTM transport is found to be significant in higher ν_* scenarios (low temperature and/or high Z_{eff}), as described in detail in [17]. Electron temperature gradient (ETG) driven turbulence is also important, particularly toward the pedestal top where $\eta_e = L_{Te}/L_{ne}$ is large. Due to their weak deviation from gyroBohm scaling, these mechanisms are expected to play a role in metal wall confinement in AUG (high ρ_*) in addition to JET and to produce similar trends.

A major outcome of this work is the identification that in a comparatively lower ρ_* machine, ITG turbulent transport can become large, even dominant. This ITG transport deviates strongly from gyroBohm ρ_* scaling but is almost completely suppressed on smaller machines and for parameters characteristic of JET carbon (JET-C) operation. The emergence of ITG transport is due to the erosion of shear suppression with decreasing ρ_*. However, for a given shearing rate, ITG transport can be suppressed when ITG growth rates are decreased, for instance, via ion dilution with a low-Z impurity ($Z_{eff} \lesssim 2$), thus enabling shear suppression at low ρ_*. Because of the emergent nature of this breakdown of shear suppression, i.e. because it is expected to have an impact only in the unique JET-ILW parameter regime, our theory is consistent with experimental ρ_* scalings of pedestal structure and confinement [20–24]. Indeed, our transport calculations match the scalings observed in JET dimensionless ρ_* scans [24], deviating only at lower ρ_* (beyond the range considered in [24]) in the high current and magnetic field regime that has proven particularly challenging for JET-ILW.

Due to an unfavorable ρ_* dependence of $E \times B$ shear rates, the trends observed on JET-ILW may be a nascent manifestation of a fundamental challenge that will be further amplified on ITER. Therefore, we hope that this work will serve as a touchstone guiding further study (both experimental and computational) seeking to verify or contradict the theories propounded in this paper. In synergy with such initiatives, this framework may guide the identification of operational

regimes that allow for the recovery of good confinement on JET and support the achievement of high fusion gain on ITER. Potential avenues along these lines are discussed throughout the paper.

This paper complements [17], which demonstrates agreement between gyrokinetic simulations and experimental power balance for a representative JET-ILW discharge, and [25, 26], which studies for ITER-like parameters (notably low ν_* and ρ_*) many of the same effects described in this work.

The paper is outlined as follows. Section 2 reviews the main JET-ILW experimental observations related to confinement degradation. Section 3 outlines the interplay between peeling ballooning stability and drift-type transport, highlighting the impact that limits on pedestal temperature can have on confinement. In section 4 we briefly review some of the basic physics underlying the simulation results. Section 5 describes in detail the models, assumptions, methods, and numerics underlying our simulations. In this section we are careful to outline many numerical details with the goal of laying a foundation for increasingly comprehensive and rigorous modeling of pedestal turbulent transport. Section 6 summarizes the results of [17], which describes the detailed modeling of JET discharge 82 585 and demonstrates good agreement between our gyrokinetic simulations and experimental transport levels. The major results of the paper are reported in section 7, which presents an extensive exploration of the JET-ILW parameter space and demonstrates ways in which this transport-oriented framework provides potential explanations for the major JET-ILW observations. A summary and discussion, including possible avenues to pursue experimental tests, are provided in section 8.

2. JET-ILW observations

The installation of the ITER-like wall was motivated by the need to study material erosion and tritium retention in preparation for ITER [8]. The ILW divertor is composed of tungsten, whose high temperature threshold for melting and resistance to sputtering make it a promising candidate as a reactor material [26]. Moreover, in comparison with carbon (the previous wall material), tungsten is less prone to tritium retention, which would be unacceptable at high levels under reactor conditions for reasons related to both fuel-supply and safety [26]. In this context, the implementation of the ILW has been successful; early JET-ILW campaigns demonstrate a reduction in long-term deuterium retention by an order of magnitude in comparison with carbon operation [8].

The challenge of operating with high-Z materials like tungsten lies in the potency with which high-Z impurities radiate when contaminating the core plasma. Tungsten-contaminated JET discharges are prone to gradually increasing energy losses from core radiation, often resulting in disruptions. Increased gas puffing is necessary to control tungsten contamination. Moreover, the use of a beryllium chamber results in much purer plasmas ($Z_{eff} \sim 1.2$ in comparison with $Z_{eff} \sim 2$ typical of carbon). However, these discharges can exhibit a substantial loss of confinement, manifested almost entirely through a decrease in pedestal-top temperature. In this section we review the major JET-ILW observations associated with this striking

change in pedestal structure in order to provide context for our subsequent presentation of gyrokinetic simulation results.

The most obvious constraint enforced by ILW operation is the need for gas puffing in order to prevent tungsten contamination. Gas puffing has long been known to degrade confinement (although the mechanism has not been well-understood) and is surely a substantial player in JET-ILW challenges. The present work offers new insights into mechanisms underlying the deleterious effects of gas puffing on transport. However, gas puffing alone cannot explain most of the JET-ILW confinement puzzles. For example, baseline high-triangularity JET-ILW discharges consistently underperform JET-C discharges for a given fueling rate (see figure 3(a) in [28]). Consequently, we also identify transport dynamics unrelated to gas puffing.

We review here the main observations related to JET-ILW confinement:

(1) ILW operation severely constrains the pedestal-top temperature. In some cases, this can be partially compensated for with higher pedestal density so that similar pressure-defined MHD limits and confinement levels are attainable.

(2) Impurity seeding (using nitrogen at the level of $Z_{eff} \lesssim 2$) facilitates a partial recovery of confinement and relaxes, to some degree, the strong constraint on pedestal temperature. Notably, in contrast with ILW operation, carbon wall operation exhibits confinement degradation with impurity seeding. For reasons that are not fully understood, neon is ineffective as a confinement-boosting impurity.

(3) JET-ILW suffers more-severely from confinement degradation than does AUG when operating with a metal wall (all-tungsten plasma-facing components) [16]. Moreover, confinement degradation is observed most-prominently on JET-ILW above a threshold in current and magnetic field ($I \gtrsim 2.5$ MA, $B \gtrsim 2.6$ T). There are surely multiple mechanisms at play (e.g. the requirement for more aggressive gas puffing to mitigate larger ELMs in a higher-field regime, reliability of higher-power NBI heating, etc). Both of these data points related to metal-wall confinement issues are consistent with a manifestation of ρ_*-dependent effects (e.g. turbulence suppression).

A detailed gyrokinetic perspective, offering several new insights into the physical mechanisms underlying these trends, follows.

3. Connection between pedestal MHD stability, heat transport, and confinement

In H-mode discharges with type I ELMs, the pre-ELM plasma is typically found to be near the peeling ballooning (ideal MHD) stability boundary. The structure of the pedestal can roughly be characterized by the width and height of the steep gradient region of the pressure profile, the height being the key parameter for fusion performance. Peeling-ballooning stability considerations are insufficient to determine the pre-ELM state since, for example, a large range of pedestal heights are acceptable given a sufficient pedestal width. Thus a second

constraint is necessary to understand and predict pedestal structure. This second constraint is provided by the transport mechanisms operative in the pedestal. As an example, the EPED model appeals to kinetic ballooning modes (KBM)—in effect a second MHD stability constraint—as the relevant transport mechanism, and arguments have been made [13] linking KBM stability to the empirical scaling $w \propto \beta_{\text{pol}}^{1/2}$, where w is the pedestal width in terms of poloidal magnetic flux, and β_{pol} is the pressure normalized to the poloidal magnetic field energy density.

There is experimental evidence for KBM activity in certain scenarios [29–32]. However, there are also many scenarios in which other transport mechanisms appear to be active and likely dominant. Recent AUG studies identify two classes of fluctuations that separately affect the saturation of the density and temperature profiles and have mode structures that are inconsistent with KBMs [33]. Additionally, several recent studies have found (for NSTX [34] and, notably, JET [17, 35]) that KBM is in a second stability regime—i.e. a regime where KBM is stable, and more so as the pressure gradient increases. Notably, in [17] (described in more detail in section 6), other mechanisms are shown to be sufficient to satisfy power balance in the pedestal, obviating the need for KBM.

Surely further study is needed to precisely define the scope of different transport mechanisms in limiting pedestal evolution in various machines and parameter regimes. In this paper, we study the role of drift-type, non-MHD (i.e. not KBM) transport mechanisms. There are important fundamental distinctions between an MHD-like mechanism and a drift-type mechanism. Since MHD does not distinguish between density and temperature, such transport mechanisms are sensitive only to the pressure gradient and robustly transport both particles and heat. In contrast, drift-type mechanisms are sensitive to differences between density and temperature gradients. In fact, the drive dependencies for the two classes of instabilities can work in opposite directions, as in the case when an $\eta = L_n/L_T$ driven drift-type instability is preferentially destabilized by a decrease in density gradient, whereas an MHD-type mechanism is stabilized. Additionally, Drift-type mechanisms are, in principle, unconstrained regarding the relative proportion of heat and particle transport.

For the scenarios studied in this paper, the relevant instabilities are driven by temperature gradients and produce robust heat flux but little particle flux. Such mechanisms are consistent with recent JET-ILW observations [18], which show that the temperature pedestal often saturates midway through the ELM cycle, while the density pedestal evolves unconstrained until the ELM crash. Such a scenario, wherein the temperature gradient is fixed and the pressure gradient increases (via the density profile), is difficult to reconcile with a KBM-like mechanism, which should only be triggered when the pressure gradient reaches a certain threshold, at which point the gradient would remain fixed it at a critical value.

Although drift-type transport mechanisms are not necessarily inconsistent with the $w \propto \beta_{\text{pol}}^{1/2}$ scaling, they are likely at play in situations where clear deviation from such a scaling is observed. For example [4], describes a JET-ILW fueling

scan over which the pedestal broadens by a factor of two but does not increase in height (i.e. there is no corresponding increase in β_{pol}). Over this fueling scan, which is conducted at constant heating power, the temperature pedestal broadens and becomes less steep—a result that clearly demonstrates (simply by the definition of heat diffusivity $\chi = \frac{Q}{n\nabla T}$, where Q is the heat flux) an increase in heat transport.

As another illustration of the interplay between MHD stability and transport [15], nicely characterizes the effects of an outward shift of the density pedestal. Two discharges are compared, which have different fueling rates, resulting in a relative shift between the density and temperature pedestals. In the high-fueling discharge, 40% more heating power is necessary in order to achieve the same stored energy. In other words, MHD stability accommodates the same stored energy in the two discharges, but the corresponding confinement time is lower in the high-fueling discharge, indicating increased transport. Framed differently, at constant heating power, the high-fueling discharge achieves lower stored energy, again implying a loss of confinement and a corresponding increase in transport. In this paper we discuss in detail the routes by which such increased transport can occur.

We note in passing that ELMs are observed in some JET-ILW discharges that do not appear to align with peeling-ballooning stability limits [5]. Although we have not pursued the possibility in detail, it is plausible that transport mechanisms like those described in this paper are related to such anomalous ELM behavior. Indeed, [19] proposes the possibility of ELMs triggered by the interplay between drift-type instabilities and critical values of flow shear rate.

As discussed above, a distinguishing characteristic of JET-ILW operation is the inability to reach high pedestal temperatures that were previously accessible for JET-C. In a case where the temperature is constrained but the density is not, one might assume that a shortfall in temperature could be compensated for with increased density, thereby reaching the same MHD limits and maintaining confinement. Interestingly, certain JET-ILW discharges appear to follow this trend (see figure 11 in [6]): as nitrogen seeding is increased, higher pedestal temperatures become accessible in concert with a decrease in pedestal density so that pre-ELM pressure remains constant. However, a deficiency in temperature can in fact result in substantial consequences for confinement and fusion gain:

(1) First, a temperature deficit will generally translate into less-favorable peeling-ballooning stability as, for example, in the high-triangularity scenario studied in [5]. Due to their low temperature (and corresponding low bootsrap current), such JET-ILW discharges are pinned to the low-current region of parameter space in the peeling-ballooning stability diagram (see figure 2 in [5]), and precluded from reaching the high current, steep pressure gradient corner (i.e. high stored energy) of the diagram that would otherwise be accessible in a high triangularity discharge. The result is a substantial reduction in confinement.

(2) A temperature limitation would directly impact confinement in any scenario where there is a constraint on the

density, for example regimes approaching the Greenwald limit or L-H power threshold; in such scenarios, a density limit precludes a compensation for low temperature via increased density.

For the following two examples, consider two discharges having the same pressure (stored energy) and differing (in terms of engineering parameters) only in their relative temperatures and densities.

(3) In the context of a JET DT campaign, the fusion cross section is sensitively dependent on temperature. Consequently, despite having the same confinement time, the higher temperature discharge will result in greater fusion gain.

(4) Due to the $n^{0.4}$ density dependence of the H98 confinement time scaling (while there is no explicit dependence on temperature), the higher density discharge will have a lower H-factor; an increase in density at the expense of temperature will leave the raw confinement time unchanged while increasing the H98 confinement time, thus reducing the H-factor.

Clearly, a composite picture that includes both peeling ballooning stability and transport is necessary to fully characterize pedestal dynamics. In many cases (notably JET-ILW), the KBM paradigm appears to inadequately describe the transport dynamics and a gyrokinetic perspective is indispensable.

4. Review of relevant microinstability physics

The results described below rely on (semi)-quantitative calculations accessible only via expensive nonlinear simulations. However, many of the major trends are determined by fundamental and transparent physical mechanisms, often reflected in the linear physics. Here, we briefly review (1) some of the basic microinstability theory relevant to ITG, ETG, and MTM turbulence in the pedestal, and (2) the shear suppression mechanism underlying pedestal formation and sustenance. A summary of the major parameter dependences is shown in table 1. Although these basic physical mechanisms are well-established, nonlinear simulations are required to quantify the magnitude of these effects in the JET-ILW context and are described in section 7.

4.1. Relevant microinstabilities

ITG and ETG [36–38] instabilities are closely related (removed only by a mass-ratio-dependent scale separation) and have many of the same parameter dependences (the correspondence is near-exact in the linear physics). Of particular interest in the pedestal context is their dependence on $\eta = L_n/L_T$, the main parameter determining the instability drive (L_n and L_T are, respectively, the density and temperature gradient scale lengths). The L_n dependence is especially important in the context of gas puffing, which can strongly affect the density pedestal by shifting it outward [15, 23, 39] (thereby creating a large η region near the pedestal top) or otherwise increasing separatrix density (thereby increasing η across the pedestal). In addition to gas puffing [23, 40], identify ρ_*-dependent trends for the density pedestal width. The

Table 1. Table summarizing the main transport mechanisms and their dependences (i.e. the response to an increase in these parameters) on important JET-ILW parameters.

| | $1/\rho_*$ | Impurities | | n_{sep} | $T_{i,sep}$ |
		Z-eff	Ion dilution		
MTM	—	↑	—	—	—
ITG	↑	—	↓	↑	↓
ETG	—	↓	—	↑	↑

importance of these effects becomes readily apparent in light of the senstivity of ITG and ETG growth rates to η. In section 7.3, we quantify the sensitivity of pedestal transport to separatrix density—a test representative of several of the density pedestal variations noted here.

ETG and ITG are also affected by impurity content in similar ways. ITG growth rates are decreased via ion dilution—i.e. the contribution of kinetic ions to an instability is decreased by a factor proportional to the ratio of the ion density to the electron density. ETG growth rates are also decreased by impurities through Z_{eff}, which enters directly into the adiabatic ion response. Thus both ITG and ETG growth rates decrease in the presence of an impurity species. Considering the moderate level of impurities characteristic of JET operation ($Z_{eff} \sim 2$, $n_d/n_e \sim 0.8$, where n_d is deuterium density), one might expect a commensurately moderate impact on the turbulence. However, as will be described below, such moderate variations in impurity content can dramatically change the resulting transport (see [41, 42] for a description of recent work demonstrating a similar sensitivity of transport to ion dilution in the Cmod core plasma).

MTM [17, 43–53] instability theory is notoriously varied and complex, with several different drive mechanisms identified in the literature. Universally, however, MTM is driven by electron temperature gradients and, due to its intrinsically electromagnetic nature (relying explicitly on magnetic fluctuations) is sensitive to β. MTM is also sensitive to collisionality. The conventional MTM requires finite collisionality for instability, although recent studies have identified MTM instability in the collisionless limit [52, 53]. The MTM that we identify in the JET-ILW pedestal falls in the collisional category, being much more robust at higher collisionality. As a result, MTM is also sensitive to impurity content due to the factor of Z_{eff} in the electron collision frequency.

As an illustration of two major effects of impurities, figure 1 shows MTM (red) and ITG (green) growth rates for three scenarios: $Z_{eff} = 1$ (i.e. no impurity species), $Z_{eff} = 2$ where the role of Z_{eff} is limited exclusively to its presence in the collision frequency, and $Z_{eff} = 2$ produced by the inclusion of a kinetic impurity species. The MTM growth rates are sensitive to Z_{eff} through the collision frequency but are not sensitive to ion dilution. In contrast, ITG growth rates are sensitive to ion dilution but are not sensitive to collisionality.

4.2. Shear suppression of pedestal turbulence

A major claim of this work is that the JET-ILW pedestal lies in a parameter regime where ion-scale electrostatic transport, which is strongly suppressed at higher ρ_*, can become
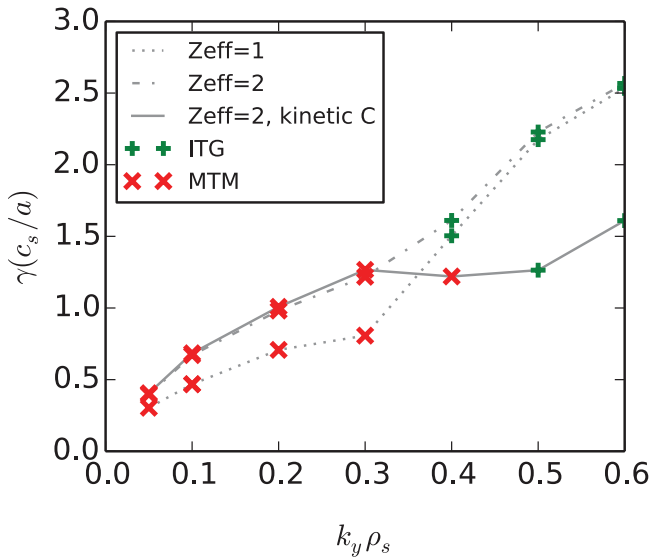
Figure 1. Linear growth rates for simulations with $Z_{eff} = 1$ and no impurity species, $Z_{eff} = 2$ with no impurity species (Z_{eff} enters only in the collision frequency), and $Z_{eff} = 2$ including a dynamic carbon species. Microtearing modes (red) are sensitive to collisionality but not ion dilution, while ITG modes (green) are sensitive to ion dilution but not collisionality.

Figure 2. Hahm–Burrell $E \times B$ shear rates across the pedestal for a scan in ρ_*. Note that shear rates decrease proportional ρ_*.

important. In this section we discuss the basic scaling arguments for why such a scenario may be expected to occur on a large machine like JET.
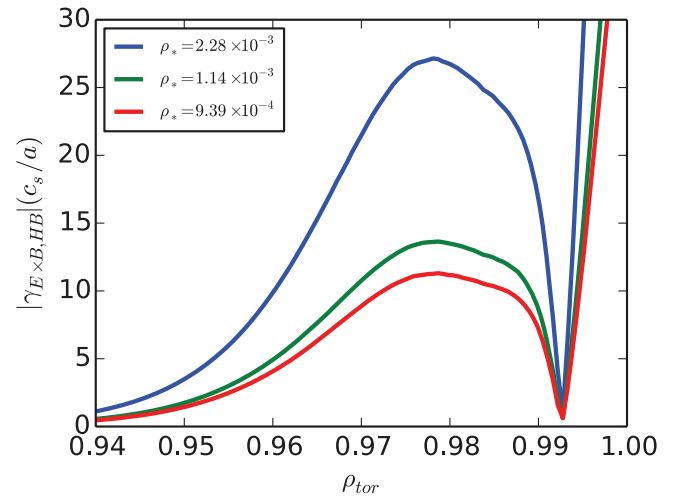
Pedestal formation and sustenance rely on the suppression of micro-instabilities by sheared $E \times B$ flows [54–56]. The ratio of the shear rate $\gamma_{E \times B} \sim \frac{d}{dr}\frac{E_r}{B_0}$ to the linear growth rates of the micro-instabilities defines the basic metric for the efficacy of the suppression mechanism. Experimentally, the radial electric field that produces the shear flow is determined by force balance with the pressure gradient [57],

$$E_r \sim \frac{\nabla P_i}{en_0}, \tag{1}$$

or more precisely, by a neoclassical version of equation (1), which distinguishes between density and temperature gradients [58]. Although a direct confirmation of this behavior is difficult from the description of E_r in [59] (which focuses mostly on zonal flows in the L-H transition), such direct measurements of E_r on JET could easily confirm equation (1). Basic manipulations of equation (1) (e.g. replacing gradients with the pedestal width, which scales like the minor radius) determine the scaling of shear suppression with ρ_*:

$$\gamma_{E \times B}\frac{a}{v_{Ti}} \sim c_0(q, \beta, \nu_*)\rho_*, \tag{2}$$

where a is the minor radius, v_{Ti} is the ion thermal velocity, ρ_* is the ratio of the ion gyroradius to the minor radius, and c_0 is an unspecified function of the other dimensionless parameters (safety factor q, β, and normalized collision frequency ν_*). Since the growth rates of micro-instabilities scale like v_{Ti}/a (variations from this are subsumed in c_0), we see clearly that the pedestal-sustaining turbulence suppression mechanism decreases with ρ_*. For sufficiently small ρ_*, then, we can expect

a serious erosion of shear suppression. Our calculations suggest that JET-ILW lies just in the regime of ρ_* where this erosion first becomes manifest. The JET-ILW pedestal, therefore, is subject to transport mechanisms that are not observed on smaller machines; many of the JET-ILW observations may originate in the insufficiency of velocity shear. Fortunately, the factor c_0 leaves room to maneuver. By identifying scenarios with low instability growth rates (i.e. sufficient ion dilution, low η, etc), shear suppression can be maintained at and beyond the JET ρ_* range.

In order to explore these effects, we examine a series of equilibria constructed to hold all dimensionless parameters (ν_*, β, q) fixed except for ρ_*, which varies from 9.4×10^{-4} to 2.3×10^{-3}, spanning a high-field ($B = 3.6$ T) JET discharge on the low side, to an AUG or DIII-D discharge on the high end. The Hahm–Burrell shear rates for these three cases are shown in figure 2, which clearly exhibits the decrease in normalized shear rates with ρ_*. The resulting nonlinear simulations will be discussed in section 7.4.

The details of the shear suppression mechanism have many features that are unique to the pedestal. For example, recent studies [17, 33, 60–62] have noted the propensity of pedestal mode structures to peak away from the outboard midplane (in contrast with typical core instabilities). Due to the strong shaping often manifest in the pedestal, there is large variation in the $E \times B$ shear rate (typically an order of magnitude) with poloidal angle (note that the potential is a flux function, resulting in a strongly varying E_r). Since the flux surfaces are most-broadly spaced at the top/bottom of the tokamak, modes that peak in these regions are potentially less-susceptible to shear suppression [25, 26]. The Hahm–Burrell shear rate is constructed to reflect the shear rate at the outboard midplane, and so a comparison of this shear rate with linear growth rates can be misleading when the modes peak at other poloidal locations. Consequently, a meaningful metric appears to be a comparison between the minimum (over poloidal angle) $E \times B$ shear rate and the growth rates of instabilities that peak away from the outboard midplane. Such considerations are discussed in [25, 26] and are a topic of ongoing study.

Independent of considerations related to shear suppression, intrinsic ρ_* effects also strongly favor increased transport with decreasing ρ_*. This manifests itself as a strong deviation from gyroBohm ρ_* scaling until a low-ρ_* threshold is reached and the local gyroBohm limit is attained [63–66]. The relevant parameter is an effective ρ_* characterized by the width of the region with strong gradients (i.e. the pedestal width, in the context of this paper) rather than a global ρ_* defined by the machine size [65]. Simulations (to be presented elsewhere) indicate that, while both intrinsic and indirect (via shear suppression) ρ_* effects are significant, the latter is the stronger effect in the pedestal.

5. Description of gyrokinetic simulations

5.1. Pedestal gyrokinetics

Before proceeding to results, this section provides a detailed description of the numerical tools and methods used in the simulations. This paper is based on simulations using the GENE code, which has been extensively benchmarked and validated for core turbulence [67, 68]. In comparison with core gyrokinetics, which has matured into a quite rigorous and reliable tool in the past decade, pedestal gyrokinetics is less established. The basic gyrokinetic assumptions of a large scale separation between (1) the gyroradius and the scale length of the magnetic field, and (2) the dynamic time scales and the gyrofrequency are both rigorously satisfied in the pedestal. Of more concern is the degree of scale separation between the gyroradius and the pedestal scale length. In smaller machines (e.g. AUG, Cmod, DIII-D), the ratio of pedestal width to gyroradius may be as small as ~10. Fortunately, for the problem at hand, JET is large enough to substantially relax this concern; for our experimental base case, the ratio of pedestal width (pedestal top to separatrix) to gyroradius is approximately 50. For this comparison, the gyroradius is calculated from the mid-pedestal temperature and the on-axis magnetic field, while the width of the pedestal as a fraction of the minor radius is assumed to roughly correspond to its width in terms of ρ_{tor} (the normalized square root of the toroidal magnetic flux). Other considerations, such as the ratio of the poloidal gyroradius to the pedestal width are also, fortunately, much more forgiving for a JET-scale device than for smaller machines.

Nonetheless, gyrokinetics has a much shorter track record in the pedestal. Some remaining weaknesses in our pedestal simulations are the inability to simulate beyond the separatrix, and the constraint to separately calculate ion and electron scale transport (as opposed to multi-scale). Moreover, in this work our nonlinear simulations are limited to a local approximation (i.e. keeping plasma parameters and gradients fixed while using Dirichlet radial boundary conditions and a box size comparable to the steep gradient region of the pedestal). While GENE has the capability to do global simulations, these remain challenging in the pedestal due to the large variations in temperature (requiring high velocity space box sizes and resolution), and the proximity to MHD limits. Here we opt for a local approximation in order to enable the extensive exploration of parameter space described in this paper. Perhaps the largest variations in pedestal parameters are the magnetic and $E \times B$ shears. We mitigate these variations by (1) including a global implementation of $E \times B$ shear (i.e. allowing the shear to vary over the box), and testing certain cases with different values of magnetic shear in order to gauge sensitivity. Moreover, targeted global tests have been performed where possible [17] and suggest that the major conclusions are not qualitatively altered by global effects.

Despite these limitations, the strengths of our simulation campaign are clear: this is among the first works modeling pedestal transport with nonlinear, fully electromagnetic gyrokinetic simulations using a realistic collision operator and experimental geometry. Notably, this is work builds on [61] wich models inter-ELM transport on AUG, and [17], which reports, for the JET-ILW base case, the first quantitative agreement between gyrokinetic simulations and experimental transport levels. This paper continues to support the position that gyrokinetics can capture important features of pedestal transport by reproducing the experimental trends observed on JET-ILW. We envision this work as part of an ongoing effort to develop increasingly rigorous and comprehensive tools for modeling the challenging edge region.

5.2. Numerical details of GENE simulations

The inputs for GENE simulations are self-consistently constructed using the equilibrium code VMEC [69] in conjunction with neoclassical formulas [58] for the bootstrap current and radial electric field. $E \times B$ shear is modeled by an advective derivative associated with the toroidal rotation (treatments differ in flux tube and global simulations in GENE [70]). The toroidal rotation is taken to be $\Omega_{tor} = \frac{E_r}{RB_\theta}$, which describes an $E \times B$ flow with a negligible parallel advective derivative. The shear rate used in GENE is a flux function defined as

$$\gamma_{GENE} = \frac{\rho_{tor}}{q} \frac{d}{d\rho_{tor}} \frac{E_r}{B_\theta R}. \tag{3}$$

Ion-scale GENE simulations take parameters at the center of the pedestal and use a box size comparable to the pedestal width (applying Dirichlet boundary conditions with sources to maintain background gradients [10]). For example, for the base case, the simulations are centered at $\rho_{tor} = 0.98$ with a box size of 0.022 of the minor radius. For other cases with different pedestal widths, the simulations are shifted and scaled accordingly. Extensive convergence tests were carried out for the MTM-dominated base case (as described in [17]) and for a case dominated by electrostatic ITG turbulence (as described in [25, 26]). Typical resolution is (256, 80, 48, 16) gridpoints in the $(x, z, v_\parallel, \mu)$ coordinates. MTM turbulence was observed to peak at low k_y (simulations converged for $k_{y,min}\rho_s = 0.018$), while the spectrum of electrostatic turbulence typically extends to higher k_y (requiring $k_{y,max}\rho_s \sim 1.5 - 2.0$). The simulations described in this paper have some minor differences (translating into minor quantitative changes) with those in [17]; we use $E \times B$ shear that varies over the box (instead of a constant local value), and we have improved the extraction of geometric coefficients from magnetic equilibria.

ETG simulations are limited to electron scales and employ an adiabatic ion approximation. Typical resolution (established by convergence tests) is 384,48,16 grid points in the $z, v_\parallel, \mu$ coordinates, with a radial wavenumber grid resolving from $k_{x,\min}\rho_s = 2.15$ to $k_{x,\max}\rho_s = 138$ and a wavenumber grid in the y coordinate resolving from $k_{y,\min}\rho_s = 5$ to $k_{y,\max}\rho_s = 235$. As discussed in more detail in [17], several factors (e.g. the fact that ETG fluctuations are isotropic and the ion-scale turbulence is dominated by background shear rather than zonal flows) suggest that multiscale effects are plausibly minor in a pedestal scenario, although a more-conclusive evaluation would require authentic multi-scale simulations that are beyond the scope of this work.

6. Detailed modeling of JET discharge 82 585

In order to make firm contact with the JET-ILW experimental conditions, we studied in detail the micro-instabilities and resulting transport for the pre-ELM profiles and equilibrium from JET pulse 82 585 described in [4] ($I = 2.5$ MA, $B = 2.7$ T, triangularity $\delta = 0.38$ $Z_{eff} \approx 1.2$). The density and temperature profiles for this discharge are labeled 'BASE' in figure 3, denoting this discharge as a base case which we modify in a controlled fashion in order to explore various effects. All (base and modified) discharges are simulated for two values of Z_{eff}: no impurity $Z_{eff} = 1$, and impurity seeded $Z_{eff} = 2$; in the latter, a dynamic impurity species is included to calculate ion-scale simulations, and an appropriate Z_{eff} is used in evaluating adiabatic response for ETG simulations.

The details of this study are found in [17], which we briefly review in order to set the stage for the following sections. Local and global linear simulations indicate that microtearing modes are the dominant ion-scale instability in the pedestal, whereas kinetic ballooning modes (KBM) are observed only in the local limit and only in a narrow region near the separatrix. In order to gauge sensitivity, we produced a scan of pedestal β by self-consistently constructing global equilibria while varying pedestal top temperature. KBM are observed to dominate at low β (approximately 60% of the nominal experimental point) but are stabilized with increasing β. In contrast, MTM becomes prominent just below the experimental operating point and dominates over a progressively broader radial region of the pedestal. This is consistent with JET-ILW being in a second-stability regime for KBM (as also concluded in an analysis of pedestal scenarios for JET-C [35] and NSTX [34]). These trends are even more pronounced in global calculations.

This linear picture is reinforced by nonlinear simulations, which showed MTM producing the bulk of the heat flux in the steep gradient region and, together with ETG transport and neoclassical transport, quantitatively accounting for experimental power balance. MTM turbulence is dominant in the steep gradient region, while ETG transport dominates toward the pedestal top where η_e is large. In this region—inner and central pedestal—the combination of ion-scale (mostly MTM) transport, ETG transport, and neoclassical transport was sufficient to match experimental power balance with only minor modifications to input parameters (10% increase to the

electron temperature gradient). Similar simulations underpredict the transport very near the separatrix (where many factors, including proximity to SOL, introduce severe uncertainties in the calculation).

For the steep gradient region (centered at $\rho_{tor} = 0.98$), the contribution from various transport mechanisms is shown in the first column of figure 4, where red denotes ion-scale electromagnetic transport, blue denotes ion-scale electrostatic transport [dark blue for ions and light blue for electrons], gray denotes neoclassical transport, and black denotes ETG transport (the other columns will be explained in later sections). The electromagnetic component accounts for the bulk of the ion-scale heat flux (a clear signature of MTM turbulence), but the simulations also identify a non-negligible—37%—contribution from the electrostatic channel. As will be described in detail below, the electromagnetic and electrostatic components (roughly corresponding to MTM and ITG mechanisms, respectively) have distinct parameter dependences (related to collisionality, $E \times B$ shear rate, and ion dilution) that produce dynamics consistent with several JET-ILW trends.

The transport phenomena identified here are uniquely consistent with recent JET-ILW observations that in certain discharges the temperature pedestal saturates midway through the ELM cycle while the density profile evolves unconstrained until the ELM crash [18]. Our success in modeling this base case serves as a foundation for an exploration of the broader JET-ILW parameter space described below.

## 7. Gyrokinetic insights into JET-ILW trends

In this section we describe GENE simulations based on several parameter variations designed to explore (1) the JET-ILW pedestal temperature limitations, (2) the beneficial effects of impurity seeding, (3) the effects of gas puffing, and 4) ρ_* effects related to shear suppression. The parameters for these pedestal variations are summarized in table 2 and representative profiles are shown in figure 3. Note that JET discharge 82 585, which was analyzed in detail in section 6, is labeled as *Base*.

7.1. (In)accessibility of high temperature pedestals

Having established in section 6 the capacity of our tools and methods to realistically model JET-ILW pedestal transport for a representative discharge, we now address the question of why JET-ILW has not been able to access the previously high JET-C pedestal temperatures. We proceed by constructing higher temperature pedestal scenarios and characterizing the resulting transport. We first examine a case (labelled T2 in figure 3 and table 2), with a pedestal temperature twice that of the base case and a slightly reduced pedestal density. This case is designed to roughly correspond to a representative JET-C discharge (see, e.g. figure 1 in [5], figures 5 and 9 in [6], figure 7 in [8], etc.). In conjunction with the modifications to temperature and density, which result in a net ~40% increase in β, we also slightly broaden the pedestal by a factor proportional to $\beta^{1/2}$ (note that although the $\beta^{1/2}$ is often not
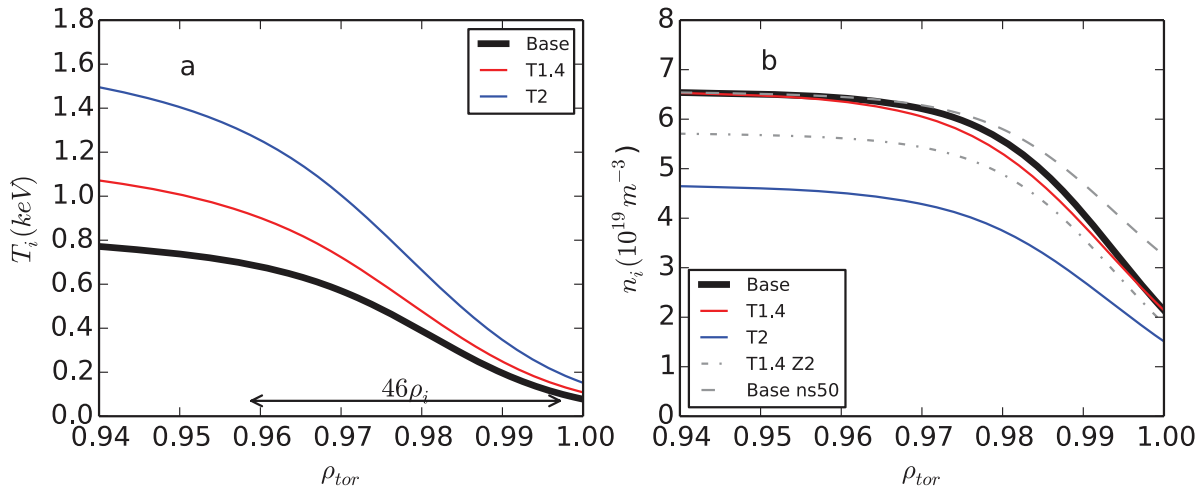
Figure 3. Temperature and density profiles representative of the parameter variations examined, corresponding to several of the cases listed in table 3. The profiles for JET discharge 82 585 are labelled 'Base'. For reference, the arrow at the bottom of the temperature plot denotes that the pedestal for the base case is 46 gyroradii wide (with the gyroradius calculated at $\rho_{\text{tor}} = 0.98$).
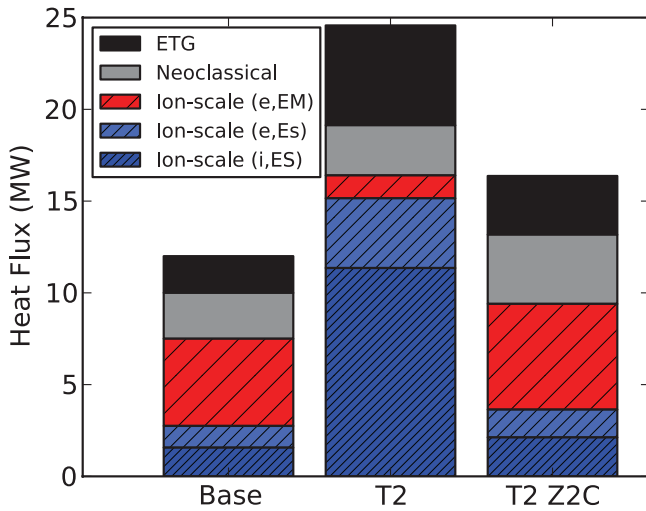
Figure 4. Contributions to the heat transport (neoclassical flux in gray, ETG transport in black, electromagnetic ion-scale transport in red, electrostatic ion-scale transport in blue (light blue for electron and dark blue for ion)) for the base case, a high temperature case (T2), and the high temperature case including a kinetic carbon species (T2 Z2). This is consistent with JET-ILW observations that high temperatures are inaccessible without the inclusion of a low-Z impurity.

clearly manifest on JET-ILW [4], from a very basic conceptual level, an increase in β must be matched by some increase in pedestal width on the grounds of MHD stability).

The resulting transport for this high temperature case is shown in the second column of figure 4. The ES and EM contributions are produced in the same ion-scale simulation, but are generally attributable to separate mechanisms, namely ITG turbulence and microtearing turbulence respectively. The most striking change in going from the base case to the high-temperature regime is a drastic increase in total transport, largely in the ES channel. The EM component of the transport is sharply decreased due to a decrease in collisionality.

Several of the important (from a gyrokinetic perspective) parameters for this transition from low (base case) to high (T2) temperature are shown in table 3. Note that the gradient

scale lengths are basically unchanged. The major changes in transport are attributable to a few basic transitions. First, there is a large decrease in collision frequency (see also table 1), which weakens microtearing turbulence. Regarding the ES transport, the increase in pedestal width substantially decreases the $E \times B$ shear rate (which scales like the square of the inverse pedestal width), allowing more ES transport. Moreover, the increase in temperature results in a much higher gyroBohm heat flux ($Q_{\text{GB}} = \rho_*^2 c_s n_0 T_0$), which translates into more transport for a given level of gyroBohm normalized turbulence. These latter effects conspire to make our prospective high-temperature pedestal inaccessible in a 15 MW-powered discharge, consistent with JET-ILW observations.

We note also that the increased temperature results (via reduced collisionality) in a stronger bootstrap current and by extension reduced magnetic shear (see figure 5). In the context of the turbulent transport described here, tests indicate that this effect is less significant than the transitions described above (although the consequences for MHD stability are certainly not negligible [6]).

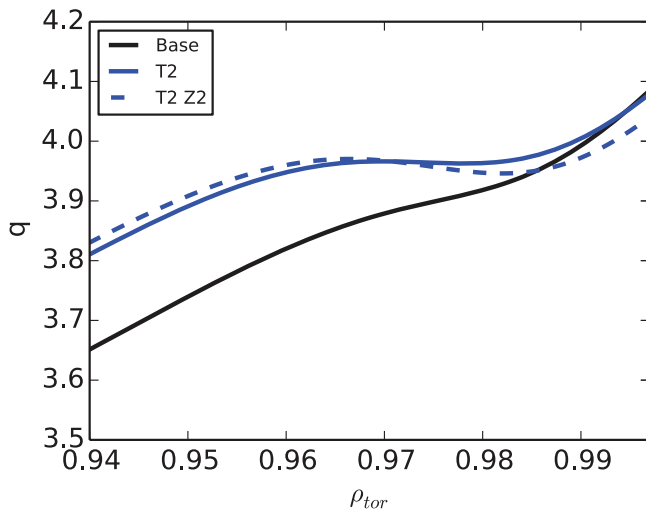## 7.2. Impurity seeding as a mechanism for confinement recovery

We are now left with the question of why high temperature pedestals were accessible for JET-C and the related question, why they can be partially recovered with N impurity seeding. In order to explore this, we add a dynamic impurity species to our simulations at the level of $Z_{\text{eff}} = 2$. Self-consistent equilibria are constructed that match the total pressure profile of the corresponding $Z_{\text{eff}} = 1$ case while varying the density profiles to satisfy quasineutrality. The major mechanisms by which this affects the turbulence are ion dilution (see, e.g. the resulting ion density profile for case T1.4 Z2 in figure 3), and the Z-effective dependence of the collision frequency $\nu_e \propto Z_{\text{eff}}$. As will be seen, the former strongly decreases the ES (ITG and ETG) transport, while the latter enhances EM (MTM) transport.

Table 2. Table showing the pedestal top and separatrix temparatures (in keV) and densities (in 10^{19} m^{-3}) along with Z_{eff}, ρ_*, ν_{*e}, and β_{e} for the cases described in the text. The major parameter variations are illustrated also in figure 3.

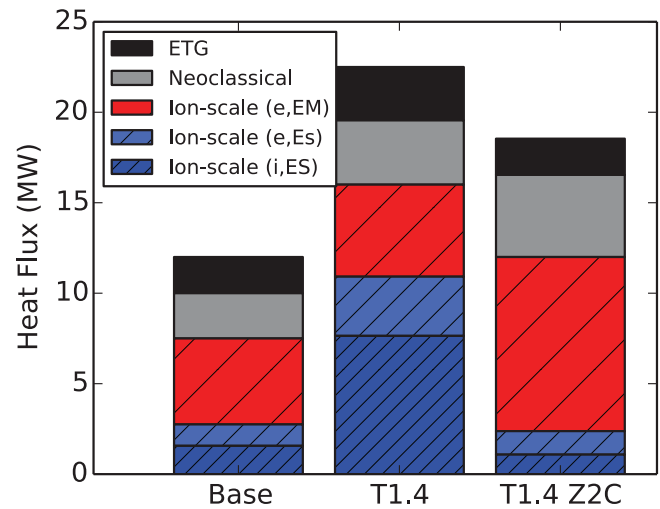| Case	T_{ped}	$n_{\text{i,ped}}$	n_{sep}	Z-eff	ρ_*	ν_{*e}	β_{e}
Base	0.65	6.45	2.14	1.0	1.14×10^{-3}	0.711	2.27×10^{-3}
Base ns50	0.65	6.45	3.25	1.0	1.14×10^{-3}	0.711	2.27×10^{-3}
Base high ρ_*	0.434	5.30	1.75	1.0	2.28×10^{-3}	0.711	2.27×10^{-3}
Base low ρ_*	0.788	9.46	3.14	1.0	9.39×10^{-4}	0.711	2.27×10^{-3}
T2	1.27	4.56	1.51	1.0	1.6×10^{-3}	0.146	3.23×10^{-3}
T2 Z2	1.27	3.93	1.32	2.0	1.6×10^{-3}	0.292	3.23×10^{-3}
T2 high ρ_*	0.842	3.79	1.26	1.0	3.2×10^{-3}	0.146	3.23×10^{-3}
T2 Z2 high ρ_*	0.842	3.28	1.10	2.0	3.2×10^{-3}	0.292	3.23×10^{-3}
T1.4	0.91	6.45	2.14	1.0	1.35×10^{-3}	0.381	3.23×10^{-3}
T1.4 Z2	0.91	5.56	1.87	2.0	1.35×10^{-3}	0.762	3.23×10^{-3}

Table 3. Table showing gyrokinetic inputs and other parameters for the base, T2, and T2 Z2 cases. Density is in units of 10^{19} m^{-3} and temperature in keV.

Case	ρ_{tor0}	T_{e}	n_{e}	a/L_{Te}	a/L_{ne}	q_0	$\hat{s}$	γ_{ExB} (avg)	$Q_{\text{GB}}V'$(kW)
Base	0.98	0.39	5.57	52.9	18.1	3.92	1.1	2.08	39.3
T2	0.978	0.73	3.89	48.4	17.2	3.96	-0.015	1.3	135
T2 Z2	0.978	0.75	4.27	48.0	16.7	3.95	-0.48	1.35	157
T1.4	0.978	0.53	5.5	48.6	17.0	3.93	0.36	1.22	83.7
T1.4 Z2	0.978	0.54	6.0	48.4	16.7	3.94	0.12	1.27	95.4

Figure 5. Profiles of safety factor q for the base, T2 and T2 Z2 cases.

Figure 6. Contributions to the heat transport (neoclassical flux in gray, ETG transport in black, electromagnetic ion-scale transport in red, electrostatic ion-scale transport in blue [light blue for electron and dark blue for ion]) for the base case, a high temperature case (T1.4), and the high temperature case including a kinetic carbon species (T1.4 Z2). The T1.4 case is constructed to be a ν_* similarity scan (holding all dimensionless parameters constant except ν_*) in comparison with the T2 case. The trend is the same (albeit weaker) as in figure 4.

The resulting transport for the case T2 Z2C ($Z_{\text{eff}} = 2$ with carbon) is shown in the third column of figure 4: the ES and ETG transport are strikingly reduced from the $Z_{\text{eff}} = 1$ case. The net result is a decrease in transport from $\sim$25 to $\sim$16 MW, consistent with JET-ILW observation that high temperature pedestals are accessible when operating with a low-Z impurity at the level of $Z_{\text{eff}} \lesssim 2$. We note also that impurity seeding appears to have beneficial effects on the density profile as described in [38].

The re-emergence of MTM with the added impurity species suggests a tradeoff between the benificial effect of ion-dilution on the ES transport and the enhancement of EM transport via the effect of increased collisionality on MTM. In order to explore this in more detail we study another case,

labeled T1.4, which has a temperature profile increased by a factor of 1.4 from the base case while maintaining the base case density. By construction, T1.4 differs from T2 (in terms of dimensionless parameters) mostly in ν_* (see tables 2 and 3—note also a small difference in ρ_*). The resulting transport is shown in figure 6. Once again, the high temperature case produces a large increase in transport (slightly lower than T2), attributable largely to the electrostatic component.
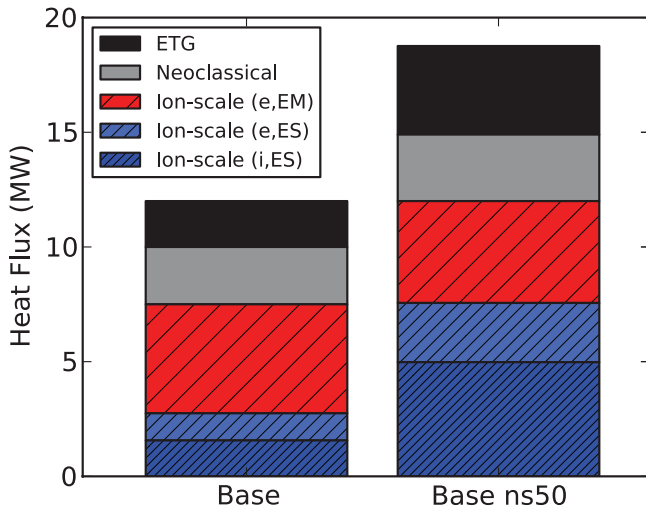
Figure 7. Contributions to the transport for the base case (left) and a case (Base ns50) deviating only by a 50% increase in separatrix density. The increase in separatrix density boosts ETG and ITG transport via an increase in η.

The corresponding kinetic carbon case—T1.4 Z2C—also exhibits a sharp reduction of ES transport with the addition of an impurity species. However the total transport reduction is less striking in T1.4 than T2 due to an enhancement of the EM component. This is consistent with the unfavorable ν_* scaling identified in [24], although the effect cannot be clearly disentangled from MHD stability considerations.

Similar to the base case, these simulations of impurity-seeded scenarios are dominated by the EM component (i.e. MTM) and have only a small contribution from the ES component. The prominence of MTM in these scenarios is consistent with the observation that impurity seeding degrades confinement: always in JET-C discharges and above a threshold in JET-ILW discharges (see figure 9 in [6]). Within our gyrokinetic picture, above a certain level, additional impurity content no longer substantially suppresses the ES transport via ion dilution but further exacerbates MTM by increasing collisionality.

Thus far we have focused on ion-scale transport. However, the same trends are apparent in the ETG transport (see figures 4 and 6): higher temperature substantially enhances the ETG component (due to the change in the gyroBohm factor), while the inclusion of an impurity species decreases ETG transport due to Z_{eff}, which enters directly into the adiabatic response. These ETG dynamics become the dominant factor at high ρ_* where higher shear rates suppress the ion-scale contribution (see section 7.5 for more detailed discussion).

We have tested both nitrogen and carbon as impurity species, and find little difference between the two (as may be expected from the small difference in atomic number). Ongoing work is examining the effect of various other impurity species. There is some scope for a transport-oriented explanation for the ineffectiveness of neon as an impurity species. For a given level of ion dilution, a higher-Z impurity produces higher Z-effective.
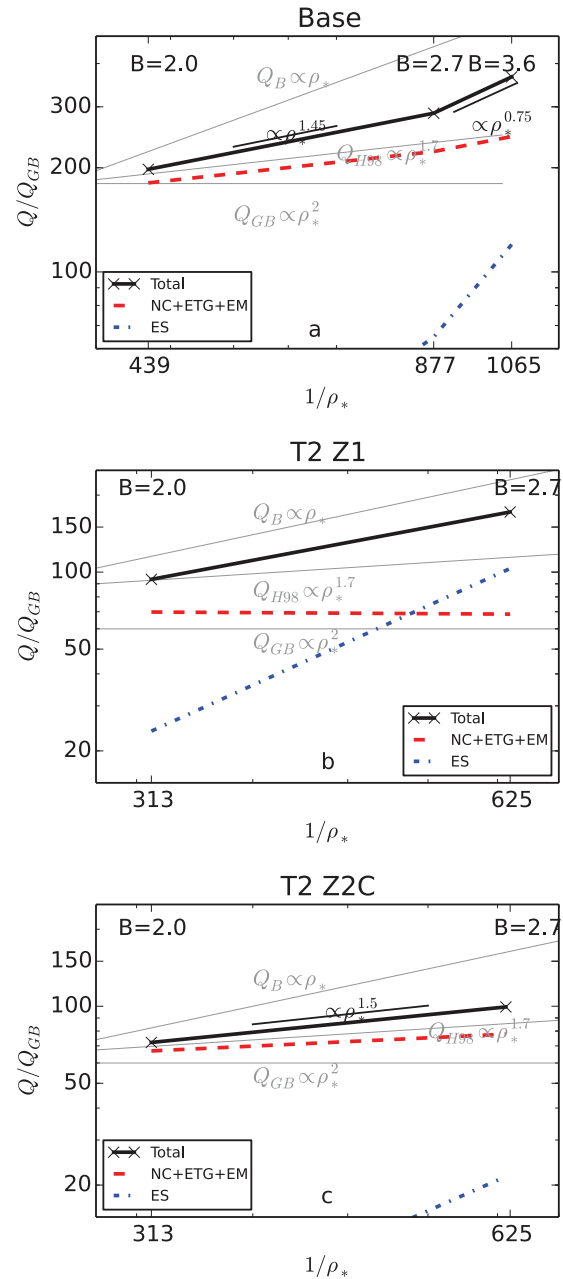
Figure 8. GyroBohm normalized heat fluxes for ρ_* scans of the base case, the T2 case, and the T2 Z2 cases. For reference, gyroBohm, Bohm, and H98 scalings are shown in gray. The combination of neoclassical, ETG, and ion-scale electromagnetic transport deviates only weakly from gyroBohm, while the ion-scale electrostatic transport deviates strongly in all cases due to the erosion of shear rates with ρ_*. The net ρ_* scaling for both the T2 Z2 and experimental base cases (at higher ρ_*) matches JET-ILW observations in the same ρ_* range.

Thus, a neon-facilitated reduction of ITG transport would correspond to a higher contribution from MTM. Our simulations, however, have not clearly demonstrated this effect, and we consider this to be, at best, a partial explanation in combination with other potential dynamics (e.g. effects of neon on separatrix density or core radiation).

7.3. Effects of gas puffing

A growing body of evidence points toward the important role of the density profile in pedestal structure and transport. Separatrix density is expected to be strongly affected by gas puffing and divertor physics [39]. A likely related observation is an outward shift of the density pedestal in discharges with high gas puffing [15, 39], and more generally at low ρ_* [23, 40]. In this section, we assess the consequences of increased separatrix density, a modification representative of these variations. The simulations are based on a slightly modified equilibrium corresponding to the experimental base case with a 50% increase in separatrix density (labeled Base ns50 in table 2 and figure 3). The results are shown in figure 7, which shows a ~50% increase in total transport, attributable to sharp increases in both ETG (by a factor of ~2) and ion-scale ES transport (by a factor of ~2.5).

In both cases, the key parameter is $\eta = L_n/L_T$, which increases due to a decreased density gradient. This change in η affects both ETG and ITG turbulence in the same way—increased growth rates and transport. In addition to the η effect, the ion-scale transport can be further enhanced by a corresponding decrease in shear rate due to the strong dependence of E_r on the density gradient in neoclassical theory.

Conversely, transport can be strongly decreased by decreasing separatrix density. This has been tested explicitly in [25, 26] for ITER-like parameters. The strong dependence of transport on separatrix density (and the density profile in general) reinforces the critical role of divertor physics in mediating an increasing array of plasma constraints, and strongly points to divertor development [72–75] as a crucial emphasis of fusion research.

We note in passing that ITG is also sensitive to the ion temperature, which may deviate from electron temperature, particularly near the separatrix. Due to SOL constraints, these two parameters (separatrix density and temperature) are inter-connected in such a way that lowering separatrix density would also raise separatrix temperature, thereby doubly affecting η and pushing growth rates downwards. An examination of such effects will be a topic of future work, as we limit the present investigation to scenarios with equal ion and electron temperatures.

7.4. Shear suppression and machine-size effects

In the preceding sections we have assessed various contributions to the transport in the context of important JET-ILW parameter variations. In this section, we determine how these transport mechanisms vary with ρ_*—i.e. how these mechanisms are expected to scale to other machines, from AUG to ITER. Due to the observed insensitivity of pedestal MHD stability to ρ_* [20–24] (in contrast with ν_* and β), dimensionless ρ_* scans like those described here provide a clean validation test that avoids conflating transport physics and MHD stability.

We identify two classes of transport mechanisms—one that has a ρ_* scaling consistent with historical observation, and a second transport mechanism with an extremely unfavorable ρ_* scaling that emerges only in a JET-ILW-like parameter regime. The existence of this second mechanism has potentially profound consequences for fusion, and compels a close examination (both experimental and computational). We emphasize that both classes of transport are subject to the trends described above (relating to impurity seeding and gas puffing), thus supplying potential mechanisms for any metal-wall scenario (AUG or JET). However, the non-gyroBohm mechanism is limited to the JET-ILW parameter regime (i.e. low ρ_* and $Z_{eff} \sim 1$) and is proposed here as a unique contributor to JET-ILW confinement challenges, in particular in the high current (low ρ_*) regime where confinement degradation appears to be more severe.

GyroBohm scaling can be conceptualized, within the framework of a diffusive random-walk, as arising from a process with a gyro-radius step size and a drift frequency time scale, producing a heat flux scaling roughly like $Q_{GB} \sim \rho_s^2(c_s/a)\nabla n_0 T_0 \sim \rho_*^2 c_s n_0 T_0$, which is the normalization used in GENE and the figures discussed below. GyroBohm scaling is appropriate for an asymptotically local transport mechanism and is followed with near-exactness for our simulated ETG and neoclassical fluxes (deviating only slightly for ETG due to Debye length effects). In the above expressions, $c_s = (T_e/m_i)^{1/2}$ is the sounds speed, ρ_s is the gyroradius at the sound speed, a is the minor radius, and n_0, T_0 are the background density and temperature, respectively. In comparison, the H98 confinement time (when manipulated into a heat flux expressed in terms of dimensionless parameters) has a dependence $Q_{H98} \propto \rho_*^{1.7}$ quite close to gyroBohm ρ_* dependence. In figure 8, gyroBohm $Q_{GB} \propto \rho_*^2$, H98 $Q_{H98} \propto \rho_*^{1.7}$, and Bohm scaling $Q_B \propto \rho_*$ will be used as points of reference in order to put the various transport mechanisms in context.

In our ion-scale simulations, the major ρ_*-dependent effect is the normalized shear rate $\gamma_{ExB}/(c_s/a)$, which as discussed in section 4.2, scales proportional to ρ_*. There is also some effect from the box size, which we keep equal to the pedestal width, arguing that the turbulence manifestly cannot have a correlation length that substantially exceeds the pedestal width. We observe that, in addition to the ETG and neoclassical mechanisms, the EM component of the ion-scale transport also deviates only weakly from gyroBohm scaling. This is consistent with the notion that microtearing physics is determined by narrow structures at rational surfaces and not strongly affected by shear flow, as discussed in [17]. In contrast, as described below, the ES component of the transport is very sensitive to shear flow and thus exhibits an unfavorable ρ_* scaling.

We examine three ρ_* similarity scans, oriented around the three cases shown in figure 4: (1) the experimental base case, (2) the high temperature T2 case, and (3) the corresponding T2 Z2C case with a kinetic carbon species. The results are shown in figure 8, which plots the total gyroBohm-normalized heat flux (black) together with the contributions from (1) transport mechanisms that deviate weakly from gyroBohm scaling (i.e. neoclassical, ETG, and ion-scale electromagnetic transport) in red, and (2) the ion-scale electrostatic transport in blue, which deviates strongly from gyroBohm scaling.

In the experimental base case scan (figure 8(*a*), three ρ_* values are chosen, which represent, respectively, a smaller
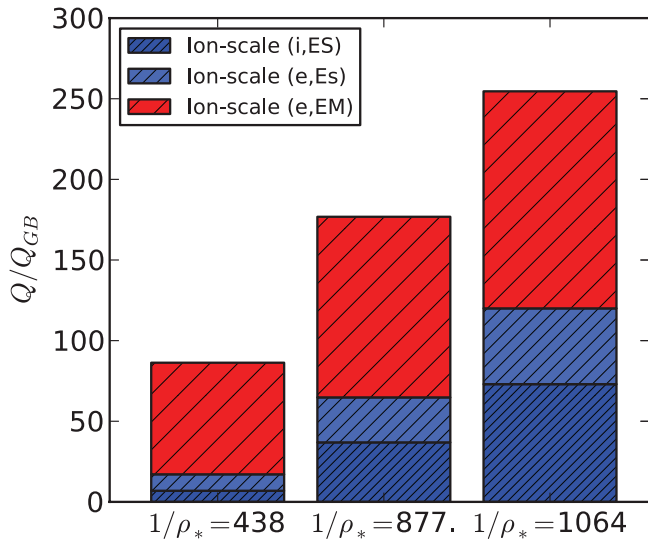
Figure 9. GyroBohm-normalized contributions to the ion scale heat flux (electromagnetic (red), ion electrostatic (dark blue)), and electron electrostatic (light blue) for a ρ_* scan based on the experimental base case (middle column). The electromagnetic component deviates weakly from gyroBohm, whereas the electrostatic components deviate strongly.

Figure 10. Contributions to the heat transport for high ρ_* cases (AUG or DIII-D) corresponding to base, T2, and T2 Z2. For these high ρ_* cases, the same trends are identified, albeit now attributable almost entirely to differences in ETG transport.

device ($1/\rho_* = 439$—e.g. AUG or DIII-D), the experimental base case ($1/\rho_* = 877$), and a JET case with a somewhat higher magnetic field ($B = 3.6$ T, $1/\rho_* = 1065$) corresponding to the apparent onset of severe confinement degradation for JET-ILW. As shown in figure 9, the ES component of the transport increases strongly with ρ_*, while the EM component increases only weakly. The combination of the EM, NC, and ETG contributions remains very close to the H98 scaling law across the scan (the ETG and NC components scale almost purely as gyroBohm). In contrast, the ES contribution scales very unfavorably and is the sole cause of the sub-H98 ρ_*-dependence. Notably, the ES component produces a significant contribution to the total transport in the same region of parameter space ($B \gtrsim 2.7$ T) where JET-ILW observes confinement degradation (see again, figure 6 in [8]).

Figure 8(*b*) shows a two-point scan for the high temperature T2 case extended up in ρ_* to a AUG/DIII-D scale device. In this high temperature (low ν_* case), the EM component is quite small, leading to a near-perfect gyroBohm scaling of the NC + ETG + EM contribution. In contrast with the other cases, the ES component is non-negligible across the scan, contributing moderately at high ρ_* (accounting for ~25% of the transport), and becoming the dominant contribution at low ρ_*. This leads to a very unfavorable ρ_* scaling, which is (coincidentally) quite close to Bohm dependence. This result indicates that for low-$Z_{\rm eff}$, low-ρ_* plasmas, high temperature pedestals are either inaccessible or only accessible with exorbitant heating power indicative of a severe breakdown of confinement.

Figure 8(*c*) shows the identical ρ_* scan differing only by the inclusion of a kinetic carbon species at the level of $Z_{\rm eff} = 2$ (recall figure 4). The ES channel is now strongly suppressed by ion dilution, restoring the scaling to a near-H98 dependence,
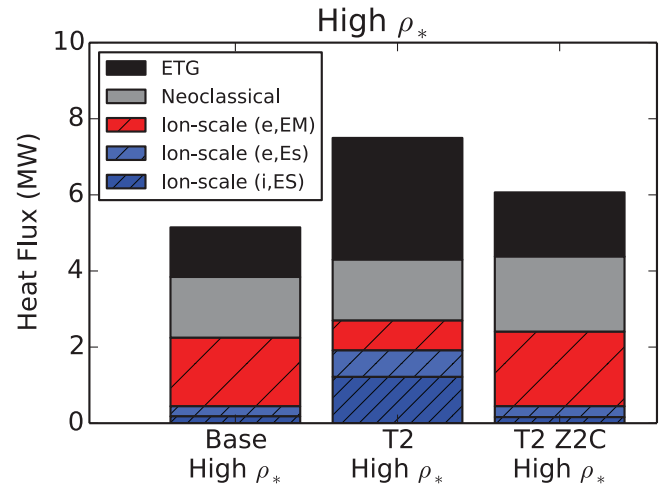
indicating that high temperature pedestals are more-accessible via impurity seeding.

Frassinetti *et al* [24] describes multiple JET-ILW dimensionless parameter scalings, identifying a $\tau \propto \sim \rho_*^{-1.5}$ scaling for the confinement time on both JET-ILW and JET-C. Although the scaling is similar for ILW and C, the ILW discharges have lower confinement across the scan, indicating a ρ_*-independent transport discrepancy. These observations are entirely consistent with the picture outlined here. As discussed above, ETG transport is a gyroBohm-like mechanism whose properties align with metal wall confinement trends (see section 7.5 for further discussion). Moreover, as shown in figure 8, our simulations exhibit ρ_* dependence matching the observations of [24], deviating only in the high temperature regime (T2 as shown in figure 8(*B*)) and at low ρ_* (in figure 8(*A*)). The former case is not observed in experiment and the latter lies beyond the ρ_* range of [24] in the high current and field regime of severe confinement degradation. In light of the results presented here, we propose a JET-ILW dimensionless ρ_* scaling study in the high current, high field regime as a test of the shear suppression dynamics described here.

To summarize, the ρ_* scans described in this section identify transport dynamics that deviate from historical observations only in the unique region of parameter space characteristic of JET-ILW—low ρ_* and $Z_{\rm eff} \sim 1$—and is thus both a plausible explanation for JET-ILW confinement degradation and consistent with established ρ_* scaling of pedestal structure. In all parameter regimes examined here, the unfavorable electrostatic ITG transport is present and exhibits similar scaling with ρ_*. Thus, ensuring acceptable pedestal transport levels will rely on understanding and reducing this transport mechanism. As described above, optimized impurity seeding and divertor operation (as manifest in the density profile) appear to be strong factors determining the base-level of ITG transport.

We note briefly that the $Q/Q_{\mathrm{GB}} \propto \rho_*^{-2}$ scaling for electrostatic transport appears to exhibit connections with basic theories of shear suppression [54] in the early literature. Such connections are being pursued and will be published elsewhere.

7.5. Impurity seeding at high ρ_*

As another view on the implications of this ρ_* dependence, figure 10 shows the high ρ_* (i.e. AUG or DIII-D scale) series of simulations analogous to those shown in figure 4. The trajectory is generally the same as that observed for JET, but with a much smaller contribution from the ion-scale transport and more specifically, the ES component. In fact, the major difference between the three cases is the ETG transport. The transition from low to high temperature produces a large increase in ETG transport almost exclusively due to the gyroBohm temperature dependence (the gyroBohm normalized ETG fluxes are very similar: 50 and 40 for the low and high temperature cases, respectively). The subsequent transition from low to high Z_{eff} affects the ETG turbulence largely through the Z_{eff} factor in the adiabatic response.

Interestingly, the same trend of confinement degradation (with a metal wall) and recovery (with impurity seeding) has been observed on AUG [71]. The combined picture illustrated in figures 4 and 10 is consistent with similar observations on both machines, with the distinction that JET is subject to enhanced transport from both electron *and* ion scales, whereas AUG is subject only to the former. A dedicated campaign comparing such dynamics on AUG and JET may be able to elucidate the ρ_*-sensitive transport mechanisms described in this paper.

8. Summary and discussion

We have carried out a campaign of gyrokinetic simulations based on high-triangularity $I = 2.5$ MA, $B = 2.7$ T JET pedestal scenarios. The goal was twofold: to elucidate the prevailing mechanisms that preclude the achievement of high temperature pedestals, and to lay a foundation for investigating achievable high temperature JET-ILW regimes. The focus was on drift-type transport phenomena, which are fundamentally different from MHD-like (e.g. KBM) transport mechanisms in that they are, among other things, driven by temperature gradients (or $\eta = L_n/L_T$) rather than pressure gradients and produce predominantly heat flux and little particle flux.

Earlier simulations modeling a representative JET discharge (first reported in [17]) served as the starting point. Linear gyrokinetic calculations of this discharge identified microtearing modes as the dominant ion-scale instability, while KBM is in a second-stability regime. Combined with significant contributions from ETG and neoclassical transport, simulations quantitatively reproduce experimental power balance. This result is consistent with the cases described in [18], wherein the temperature pedestal saturates midway through the ELM cycle while the density evolves unconstrained until the ELM crash—dynamics that are difficult to reconcile with a KBM limited pedestal.

Encouraged by the ability of the gyrokinetic calculations to reproduce the power balance, we systematically explored the most revealing regions of parameter space. The major parameter dependences are outlined in table 2. Appropriately extrapolated high temperature pedestal scenarios (like those previously accessible with JET-C) were studied in order to understand the observed constraint on pedestal temperature. The constructed high temperature scenarios exhibit a sharp increase in electrostatic (ITG and ETG) turbulent transport; the predicted transport levels exceed the available heating power implying their experimental inaccessibility. In addition to the expected temperature enhanced gyroBohm heat flux (i.e. more transport is produced for a given level of normalized turbulence), much of the excess transport could be attributed to a reduction in the $E \times B$ shear rate for a commensurately broader pedestal. The erosion of turbulent suppression by shear flows may be a major reason that JET-ILW does not achieve high temperatures.

We also find ITG turbulence is strongly decreased via ion dilution when a kinetic impurity species (nitrogen or carbon at the level of $Z_{\mathrm{eff}} \sim 2$) is included in the simulations. This finding, consistent with the higher temperatures accessible to JET-C and nitrogen seeded JET-ILW discharges, brings into focus the fact that it is the ratio of shearing rate to growth rate that determines the efficacy of the suppression of ITG-like turbulence-i.e. a decreased shearing rate can be compensated by a weaker growth rate. Likewise, ETG transport is reduced by impurities due to the presence of Z_{eff} in the adiabatic response.

Simulations are also consistent with the observed degradation of confinement with gas puffing (not unique to JET-ILW); assuming that a consequence of gas puffing is an increase in separatrix density (at fixed pedestal-top density), the resulting increase in $\eta = L_n/L_T$ greatly enhances both ion- and electron-scale transport levels. This test is also representative of related effects, such as shifted density pedestals, which create a high η region near the pedestal top and have been observed on JET-ILW and other experiments. We emphasize the crucial role of the density pedestal, as mediated by SOL and divertor physics, as a determining factor in pedestal transport. Notably, optimized divertor configurations may reconcile metal-wall constraints with low fueling levels, thereby minimizing confinement degradation.

One of the principal pursuits was to thoroughly investigate the ρ_*-dependence of pedestal transport mechanisms. An extended series of similarity scans (varying ρ_* while holding all other dimensionless parameters fixed) demonstrates $\rho*$ scaling matching historical observations in a broad region of parameter space, with strong deviations observed only in the unique unseeded JET-ILW parameter regime (low ρ_* and low Z_{eff}). In this context, we have identified two distinct classes of transport mechanisms. The MTM and ETG follow quite closely gyroBohm ρ_* scaling, and are expected to play a role in metal-wall effects observed for both AUG and JET-ILW. In contrast, electrostatic ITG turbulence exhibits strong sensitivity to $E \times B$ shear flow (which decreases with ρ_*) and thus exhibits a very unfavorable ρ_* scaling. This non-gyroBohm mechanism produces large transport levels only in the JET-ILW parameter regime and would thus predict that JET would encounter unique

challenges in metal-wall operation. Potential consequences for ITER are discussed in a separate publication [25, 26].

To succinctly summarize results: various consequences of metal-wall operation (for example, low Z_{eff} and increased pedestal $\eta = L_n/L_T$) amplify microinstability in the pedestal. These changes conspire with a decrease of $E \times B$ shear rates at low ρ_* to seriously limit pedestal temperature and degrade confinement on JET-ILW. Our study suggests that fine-tuned impurity seeding (possibly exploiting non-trivial interactions between kinetic impurities and turbulence) may lead to further JET-ILW improvements. Furthermore, this study emphatically points out that managing the divertor/SOL conditions could provide a crucial knob in the success of JET and future burning plasma devices. In particular, the density profile, as mediated by SOL conditions, is a powerful factor determining the virulence of multiple pedestal transport mechanisms.

Our simulations suggest several avenues for experimental inquiry targeted at confirming (or contradicting) the framework proposed and developed in this paper. First, we predict a transition from electron-dominated to ion-dominated pedestal heat flux as heating power is increased and/or when ρ_* falls below some threshold value. An analysis of impurity transport may be the most accessible route to identifying such a transition. Second, we predict the effects preventing high temperature pedestals to be more potent below a threshold in ρ_*. We also propose pedestal $\eta = L_n/L_T$ as a valuable metric when interpreting pedestal performance.

The theories developed in this paper are ready for (1) verification and benchmarking by further pedestal gyrokinetic simulations, and (2) experimental validation, in particular, for JET-ILW-type parameter regimes. The unfavorable ρ_* scaling of electrostatic pedestal ITG turbulence is an important verification target.

Finally, we emphasize the critical role of JET in exploring the unique pedestal dynamics described in this paper and resolving potential challenges for ITER. Future work will support such efforts by exploring via gyrokinetic simulations $Q = 1$ JET scenarios that are accessible within the constraints of the ILW.

Acknowledgments

References

[1] Philipps V.V. 2010 *Fusion Eng. Des.* **85** 1581
[2] Matthews G.F. *et al* 2011 *Phys. Scr. T* **145** 014001
[3] Giroud C. *et al* 2013 *Nucl. Fusion* **53** 113025
[4] Leyland M.J. *et al* 2015 *Nucl. Fusion* **55** 013019
[5] Maggi C.F. *et al* 2015 *Nucl. Fusion* **55** 113031
[6] Giroud C. *et al* 2015 *Plasma Phys. Control. Fusion* **57** 035004
[7] Kim H.-T., Romanelli M., Voitsekhovitch I., Koskela T., Conboy J., Giroud C., Maddison G., Joffrin E. and JET Contributors 2015 *Plasma Phys. Control. Fusion* **57** 065002
[8] Nunes I. and JET Contributors 2016 *Plasma Phys. Control. Fusion* **58** 014034
[9] Jenko F., Dorland W., Kotschenreuther M. and Rogers B.N. 2000 *Phys. Plasmas* **7** 1904
[10] Görler T., Lapillonne X., Brunner S., Dannert T., Jenko F., Merz F. and Told D. 2011 *J. Comput. Phys.* **230** 7053
[11] Connor J.W., Hastie R.J., Wilson H.R. and Miller R.L. 1998 *Phys. Plasmas* **5** 2687
[12] Huysmans G.T.A. 2005 *Plasma Phys. Control. Fusion* **47** B165
[13] Snyder P.B., Groebner R.J., Leonard A.W., Osborne T.H. and Wilson H.R. 2009 *Phys. Plasmas* **16** 056118
[14] Snyder P.B., Aiba N., Beurskens M., Groebner R.J., Horton L.D., Hubbard A.E., Hughes J.W., Huysmans G.T.A., Kamada Y. and Kirk A. 2009 *Nucl. Fusion* **49** 085035
[15] Stefanikova E. *et al* 2016 *43rd EPS Conf. on Plasma Physics (Leuven, Belgium, 04–08 July, 2016)* (http://www.eps.org/events/EventDetails.aspx?id=693990)
[16] Beurskens M.N.A. *et al*, ASDEX Upgrade Team and JET-EFDA Contributors 2013 *Plasma Phys. Control. Fusion* **55** 124043
[17] Hatch D.R., Kotschenreuther M., Mahajan S., Valanju P., Jenko F., Told D., Görler T. and Saarelma S. 2016 *Nucl. Fusion* **56** 104003
[18] Maggi C.F. *et al* 2016 *Proc. of the 26th IAEA Fusion Energy Conf. (Kyoto, Japan, 17–22 October, 2016)* (http://www-pub.iaea.org/iaeameetings/48315/26th-iaea-fusion-energy-conference)
[19] Bokshi A., Dickinson D., Roach C.M. and Wilson H.R. 2016 *Plasma Phys. Control. Fusion* **58** 75011
[20] Osborne T.H. *et al* 1999 H-mode pedestal characteristics in ITER shape discharges on DIII-D *J. Nucl. Mater.* **266–9** 131–7
[21] Urano H., Takizuka T., Kamada Y., Oyama N., Takenaga H. and The JT-60 Team 2008 *Nucl. Fusion* **48** 45008
[22] Groebner R.J., Leonard A.W., Snyder P.B., Osborne T.H., Maggi C.F., Fenstermacher M.E., Petty C.C. and Owen L.W. 2009 *Nucl. Fusion* **49** 85037
[23] Beurskens M.N.A. *et al*, The ASDEX Upgrade Team, The DIII-D Team and JET EFDA Contributors 2011 *Phys. Plasmas* **18** 56120
[24] Frassinetti L. *et al* 2017 Dimensionless scalings of confinement, heat transport and pedestal stability in JET-ILW and comparison with JET-C *Plasma Phys. Control. Fusion* **59** 14014
[25] Kotschenreuther M. 2015 *Bull. Am. Phys. Soc.* **60**
[26] Kotschenreuther M., Hatch D.R., Mahajan S., Valanju P., Zheng L., Liu X. Burning Plasmas in the High Confinement Mode and ITER *Nucl. Fusion* submitted
[27] Philipps V., Neu R., Rapp J., Samm U., Tokar M., Tanabe T. and Rubel M. 2000 Comparison of tokamak behaviour with tungsten and low- Z plasma facing materials *Plasma Phys. Control. Fusion* **42** B293
[28] Beurskens M.N.A. *et al* and JET-EFDA Contributors 2014 *Nucl. Fusion* **54** 043001
[29] Yan Z., McKee G.R., Groebner R.J., Snyder P.B., Osborne T.H. and Burrell K.H. 2011 *Phys. Rev. Lett.* **107** 055004
[30] Yan Z., McKee G.R., Groebner R.J., Snyder P.B., Osborne T.H., Beurskens M.N. and Burrell K.H. 2011 *Phys. Plasmas* **18** 056117
[31] Diallo A. *et al* and Alcator C-Mod Team 2014 *Phys. Rev. Lett.* **112** 115001
[32] Diallo A. *et al* 2015 *Phys. Plasmas* **22** 56111

[33] Laggner F.M. *et al* 2016 High frequency magnetic fluctuations correlated with the inter-ELM pedestal evolution in ASDEX Upgrade *Plasma Phys. Control. Fusion* **58** 65005

[34] Canik J.M., Guttenfelder W., Maingi R., Osborne T.H., Kubota S., Ren Y., Bell R.E., Kugel H.W., LeBlanc B.P. and Souhkanovskii V.A. 2014 *Nucl. Fusion* **53** 113016

[35] Saarelma S., Beurskens M.N.A., Dickinson D., Frassinetti L., Leyland M.J., Roach C.M. and EFDA-JET Contributors 2013 *Nucl. Fusion* **53** 123012

[36] Dorland W., Jenko F., Kotschenreuther M. and Rogers B.N. 2000 *Phys. Rev. Lett.* **85** 5570

[37] Jenko F. and Dorland W. 2002 *Phys. Rev. Lett.* **89** 225001

[38] Nevins W.M. *et al* 2006 *Phys. Plasmas* **13** 122306

[39] Dunne M. *et al* 2017 *Plasma Phys. Control. Fusion* **59** 14017

[40] Schneider P.A. *et al*, The ASDEX Upgrade Team, The DIII-D Team and JET EFDA Contributors 2012 *Plasma Phys. Control. Fusion* **54** 105009

[41] Ennever P. *et al* 2015 *Phys. Plasmas* **22** 072507

[42] Ennever P. *et al* 2016 *Phys. Plasmas* **23** 082509

[43] Hazeltine R.D. *et al* 1975 *Phys. Fluids* **18** 1778

[44] Drake J.F. and Lee Y.C. 1977 *Phys. Rev. Lett.* **39** 453

[45] Mahajan S.M., Hazeltine R.D., Strauss H.R. and Ross D.W. 1979 *Phys. Fluids* **22** 2147

[46] Applegate D.J. *et al* 2004 *Phys. Plasmas* **11** 5085

[47] Applegate D.J., Roach C.M., Connor J.W., Cowley S.C., Dorland W., Hastie R.J. and Joiner N. 2007 *Phys. Control. Fusion* **49** 1113

[48] Doerk H., Jenko F., Pueschel M.J. and Hatch D.R. 2011 *Phys. Rev. Lett.* **106** 155003

[49] Guttenfelder W., Candy J., Kaye S.M., Nevins W.M., Wang E., Bell R.E., Hammett G.W., LeBlanc B.P., Mikkelsen D.R. and Yuh H. 2011 *Phys. Rev. Lett.* **106** 155004

[50] Hatch D.R., Pueschel M.J., Jenko F., Nevins W.M., Terry P.W. and Doerk H. 2012 *Phys. Rev. Lett.* **108** 235002

[51] Hatch D.R., Pueschel M.J., Jenko F., Nevins W.M., Terry P.W. and Doerk H. 2013 *Phys. Plasmas* **20** 012307

[52] Predebon I. and Sattin F. 2013 *Phys. Plasmas* **20** 040701

[53] Terry P.W. *et al* 2015 *Nucl. Fusion* **55** 104011

[54] Zhang Y.Z. and Mahajan S.M. 1992 *Phys. Fluids* B **4** 1385
Zhang Y.Z. and Mahajan S.M. 1993 *Phys. Fluids* B **5** 2000

[55] Burrell K.H. 1997 *Phys. Plasmas* **4** 1499

[56] Terry P.W. 2000 *Rev. Mod. Phys.* **72** 109

[57] Viezzer E. *et al* and The ASDEX Upgrade Team 2013 *Nucl. Fusion* **53** 53005

[58] Sauter O., Angioni C. and Lin-Liu Y.R. 1999 *Phys. Plasmas* **6** 2834–9

[59] Hillesheim J.C. *et al* 2016 *Phys. Rev. Lett.* **116** 65002

[60] Fulton D.P., Lin Z., Holod I. and Xiao Y. 2014 *Phys. Plasmas* **21** 042110

[61] Hatch D.R., Told D., Jenko F., Doerk H., Dunne M.G., Wolfrum E., Viezzer E., Pueschel M.J. and ASDEX Upgrade Team 2015 *Nucl. Fusion* **55** 063028

[62] Xie H. and Xiao Y. 2015 *Phys. Plasmas* **22** 90703

[63] Lin Z., Ethier S., Hahm T.S. and Tang W.M. 2002 *Phys. Rev. Lett.* **88** 195004

[64] Candy J., Waltz R.E. and Dorland W. 2004 *Phys. Plasmas* **11** L25

[65] McMillan B.F. *et al* 2010 *Phys. Rev. Lett.* **105** 155001

[66] Görler T. *et al* 2011 *Phys. Plasmas* **18** 056103

[67] Navarro A.B., Happel T., Grler T., Jenko F., Abiteboul J., Bustos A., Doerk H., Told D. and ASDEX Upgrade Team 2015 *Phys. Plasmas* **22** 42513

[68] Told D., Jenko F., Görler T., Casson F.J., Fable E. and ASDEX Upgrade Team 2013 *Phys. Plasmas* **20** 122312

[69] Hirshman S.P. and Whitson J.C. 1983 *Phys. Fluids* **26** 3553

[70] Told D. 2012 *PhD Thesis* Universität Ulm

[71] Beurskens M.N.A. *et al*, The EUROfusion MST1 Team and The ASDEX-Upgrade Team 2016 *Nucl. Fusion* **56** 056014

[72] Kotschenreuther M., Valanju P.M., Mahajan S.M. and Wiley J.C. 2007 *Phys. Plasmas* **14** 072502

[73] Kotschenreuther M., Valanju P., Covele B. and Mahajan S. 2013 *Phys. Plasmas* **20** 102507

[74] Covele B., Valanju P., Kotschenreuther M. and Mahajan S. 2014 *Nucl. Fusion* **54** 072006

[75] LaBombard B. *et al* 2015 *Nucl. Fusion* **55** 053020